

The discovery and characterization of Earth-crossing asteroid 2024 YR<sub>4</sub>

BRYCE T. BOLIN,<sup>1,\*</sup> JOSEF HANUŠ,<sup>2,\*</sup> LARRY DENNEAU,<sup>3,\*</sup> ROBERTO BONAMICO,<sup>4</sup>  
LAURA-MAY ABRON,<sup>5</sup> MARCO DELBO,<sup>6,7</sup> JOSEF ĎURECH,<sup>2</sup> ROBERT JEDICKE,<sup>3</sup> LEO Y. ALCORN,<sup>8</sup>  
ALEKSANDAR CIKOTA,<sup>9</sup> SWAYAMTRUPTA PANDA,<sup>9</sup> AND HENRIQUE REGGIANI<sup>9</sup>

<sup>1</sup>*Eureka Scientific, Oakland, CA 94602, U.S.A.*

<sup>2</sup>*Charles University, Faculty of Mathematics and Physics, Institute of Astronomy, 180 00 Prague, Czech Republic*

<sup>3</sup>*Institute for Astronomy, University of Hawai‘i at Mānoa, Honolulu, HI, 96822*

<sup>4</sup>*BSA Osservatorio (K76), 12038 Savigliano, Cuneo, Italy*

<sup>5</sup>*Griffith Observatory, Los Angeles, CA 90027*

<sup>6</sup>*Université Côte d’Azur, CNRS Lagrange, Observatoire de la Côte d’Azur, F 06304, Nice, France*

<sup>7</sup>*University of Leicester, School of Physics and Astronomy, Leicester, LE1 7RH, UK*

<sup>8</sup>*W. M. Keck Observatory, Waimea, HI 96743, USA*

<sup>9</sup>*International Gemini Observatory/NSF NOIRLab, Casilla 603, La Serena, Chile*

(Received –; Revised –; Accepted –)

Submitted to ApJL

ABSTRACT

We describe observations and physical characteristics of Earth-crossing asteroid 2024 YR<sub>4</sub>, discovered on 2024 December 27 by the Asteroid Terrestrial-impact Last Alert System. The asteroid has semi-major axis,  $a = 2.52$  au, eccentricity,  $e = 0.66$ , inclination  $i = 3.41^\circ$ , and a  $\sim 0.003$  au Earth minimum orbit intersection distance. We obtained g, r, i, and Z imaging with the Gemini South/Gemini Multi-Object Spectrograph on 2025 February 7. We measured a g-i spectral slope of  $13 \pm 3$  %/100 nm, and color indices  $g-r = 0.70 \pm 0.10$ ,  $r-i = 0.25 \pm 0.06$ ,  $i-Z = -0.27 \pm 0.10$ . 2024 YR<sub>4</sub> has a spectrum that best matches R-type and Sa-type asteroids and a diameter of  $\sim 30$ -65 m using our measured absolute magnitude of  $23.9 \pm 0.3$  mag, and assuming an albedo of 0.15-0.4. The lightcurve of 2024 YR<sub>4</sub> shows  $\sim 0.4$  mag variations with a rotation period of  $\sim 1170$  s. We use photometry of 2024 YR<sub>4</sub> from Gemini and other sources taken between 2024 December to 2025 February to determine the asteroid’s spin vector and shape, finding that it has an oblate,  $\sim 3:1$  a:c axial ratio and a pole direction of  $\lambda, \beta = \sim 42^\circ, \sim 25^\circ$ . Finally, we compare the orbital elements of 2024 YR<sub>4</sub> with the NEO population model and find that its most likely sources are resonances between the inner and central Main Belt.

*Keywords:* minor planets, asteroids: individual (2024 YR<sub>4</sub>), temporarily captured orbiters, minimoons

\* These authors contributed equally to this work.

## 1. INTRODUCTION

Earth-crossing asteroids (ECAs) are asteroids whose orbital trajectories cross the Earth's coming within its 0.983 au perihelion,  $q$ , and 1.017 au aphelion,  $Q$ , distances. By definition, ECAs belong to the Apollo NEO class with semi-major axes,  $a > 1$  au, and  $q < 1.017$  au, and the Aten NEO class with  $a < 1$  au and  $Q > 0.983$  au. ECAs present scientific opportunities for detailed study of close approaching near-Earth objects (NEO, e.g., [Granvik et al. 2013](#); [Binzel et al. 2015](#)). Interactions with the Earth's tides during close-approaching asteroids can affect the structural integrity of asteroids, causing changes in their surface material properties ([Binzel et al. 2010](#)), or completely disrupt, making Earth-encounters a source of some NEOs ([Granvik & Walsh 2024](#); [Nesvorný et al. 2024](#)). Additionally, a portion of EC asteroids are a source of impacts on the Earth and the Moon affecting their total impact flux ([Mazrouei et al. 2019](#); [Cohen et al. 2023](#)). Thus, ECAs provide examples of useful study on the effect of close approaches on the physical properties of asteroids and the impact chronology of the Earth and Moon.

The majority of ECAs originate from sources in the inner Main Belt between 2.2 au and 2.5 au ([Granvik et al. 2018](#)). Asteroids leave the Main Belt due to the Yarkovsky effect causing their semi-major axes to evolve, increasing for prograde-spinning asteroids and decreasing for asteroids that are spinning retrograde ([Vokrouhlický et al. 2015](#)). As asteroids evolve in their semi-major axis due to the Yarkovsky effect, they cross resonances such as the  $\nu_6$  resonance that defines the inner border of the Main Belt at 2.2 au, the 3:1 mean motion resonance (MMR) with Jupiter at 2.5 au, and various weaker resonances located between 2.2 au and 2.5 au ([Granvik et al. 2017](#)). The interaction between the orbits of these asteroids and the resonances causes their orbits to chaotically evolve, sending them on trajectories where they can encounter the Earth ([Wisdom 1983](#); [Farinella et al. 1993](#)).

While the majority of inner Main Belt asteroids belong to the siliceous S-type group,  $\sim 20\%$  of inner Main Belt asteroids belong to the more primitive and carbonaceous C-type group ([DeMeo & Carry 2013](#)). This results in the majority of C-type NEOs originating from the inner region of the Main Belt ([Binzel et al. 2019](#)). Additionally, a considerable portion of NEOs can also belong to the X-type class, whose compositions span enstatite achondrite and metallic compositions ([Bus & Binzel 2002](#); [Avdellidou et al. 2022](#)). While the orbits of NEOs and their likely sources within the Main Belt provide constraints on their composition ([Jedicke et al. 2022](#)), the information on the composition of NEOs can be enhanced through observations covering visible and near-infrared wavelengths ([DeMeo et al. 2009](#)).

This paper discusses the discovery of ECA 2024 YR<sub>4</sub> by the Asteroid Terrestrial-impact Last Alert System (ATLAS, [Tonry et al. 2018](#)) telescope and observations taken at Gemini South and the determination of its physical shape model. We also adapt the techniques described by [Bolin et al. \(2020, 2021, 2025\)](#) of using multi-band photometry to constrain the physical and taxonomic properties of 2024 YR<sub>4</sub>. Finally, we will use the lightcurve inversion techniques established by ([Hanus et al. 2011, 2018](#)) on publically sparse and dense data to determine the spin vector and shape of 2024 YR<sub>4</sub>, and test its likely source within the Main Belt using the NEO population model ([Morbidelli et al. 2020](#); [Nesvorný et al. 2023, 2024](#)).

## 2. OBSERVATIONS

The ATLAS Chile, Rio Hurtado telescope, with Minor planet Center (MPC) observing code W68, made the first discovery observations of 2024 YR<sub>4</sub> on 2024 December 27 05:42:49 UTC as seen in

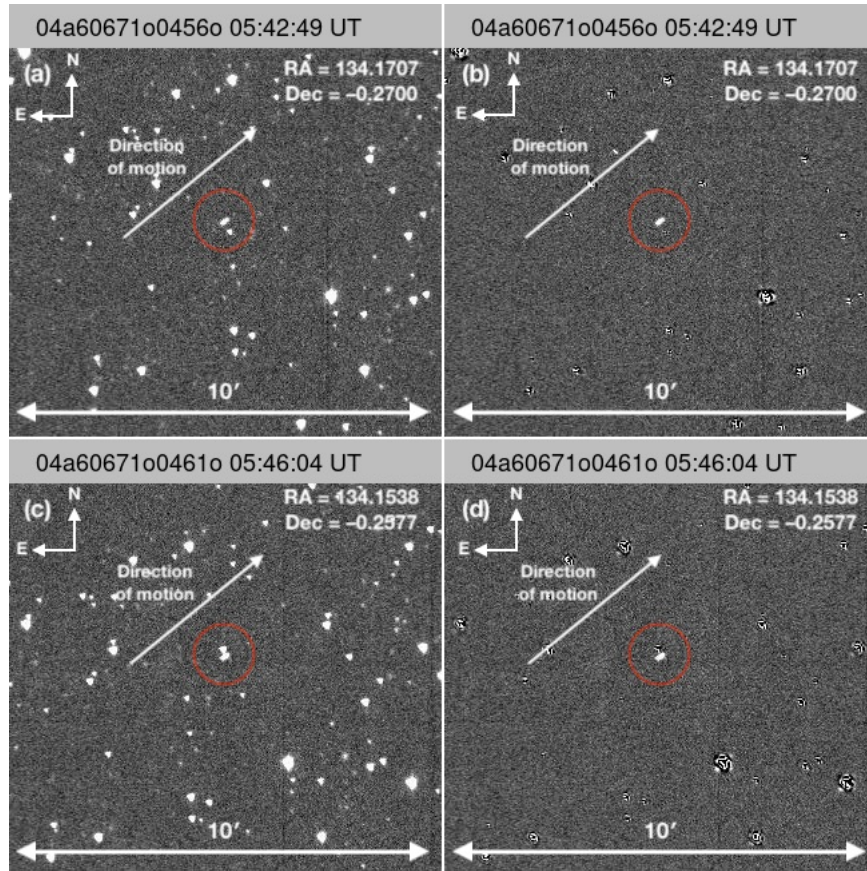


**Figure 1. Panel a:** The first of four o-band ATLAS-Chile telescope discovery images of 2024 YR<sub>4</sub> from 2024 December 27 05:42:49 UTC. The asteroid moved at a rate of 22.8 arcminutes per hour (9.11 degrees per day) in the northwest direction. The asteroid makes a  $\sim 6$  pixel trail ( $\sim 11''$ ) in the 30 s ATLAS exposures, indicated by the red circle. **Panel b:** the same as panel a but shows the image after subtracting static sources. Despite the presence of nearby stars, the asteroid is detected cleanly in the subtracted images. **Panel c:** the same as panel a, but the second of four o-band images containing 2024 YR<sub>4</sub> taken on 2024 December 27 05:46:04 UTC. **Panel d:** the same as panel c but shows the image after subtracting static sources. The asteroid was detected with an apparent magnitude of  $m=16.54$  in panel a and  $m=15.80$  in panel c. The large black areas in the subtracted images are regions of saturated pixels from bright stars. The direction of the asteroid and cardinal directions are indicated in each figure.

Panels a-d of Fig 1. The asteroid was discovered at right ascension (RA) and declination (dec) of 08:56:40.97, -00:16:11.93, and was located 0.996 au from the Sun, 0.017 au from the Earth, and at a phase angle of  $43.2^\circ$ , and an apparent magnitude of  $\sim 16.17$  in the ATLAS o-band filter (Denneau et al. 2024). The ATLAS camera has a pixel scale of  $1.86''$ , an “orange” o-band custom filter providing wavelength coverage between 560 nm and 820 nm, and an effective wavelength of 663 nm (Tonry et al. 2018). The asteroid was detected in all four o-band images taken in a 3160 s interval from 2024 December 27 05:42:49 UTC to 2024 December 27 06:35:30 UTC. The asteroid was moving northwest at  $\sim 22''/\text{min}$ , resulting in the detections forming a trail  $\sim 11''$  long (panels a-d, Fig. 1).

A director’s discretionary time request (DDT) was granted at Gemini South to observe 2024 YR<sub>4</sub> on 2025 February 7 02:23:46 UTC under program GS-2025A-DD-102 (PI: Bolin). The asteroid was located at RA, dec = 08:04:08.66, +13:33:24.31, 1.367 au from the Sun, 0.399 au from the Earth and

had a phase angle of  $14.8^\circ$  during the 2025 February 7 UTC observations. The Gemini Multi-Object Spectrograph (GMOS) instrument (Hook et al. 2004) was used in imaging mode to observe 2024 YR<sub>4</sub> in g, r, I, and Z filters. The GMOS camera comprises a  $5.5' \times 5.5'$  field of view Hamamatsu array with an effective pixel scale of  $0.08''$ . The camera was used in  $2 \times 2$  binning mode, giving an effective pixel scale of  $0.16''$ . The GMOS g, r, and i filters are equivalent to Sloan Digital Sky Survey (SDSS) g, r, and i filters with effective wavelengths of 475 nm, 630 nm, and 780 nm (Fukugita et al. 1996). A filter was used for coverage past 800 nm equivalent to the the WFCAM Z with an effective wavelength of 880 nm (Casali et al. 2007). This filter has the advantage of being equivalent to the SDSS z filter, but avoids telluric absorption features near 950 nm (Hodgkin et al. 2009). Observations of 2024 YR<sub>4</sub> were also taken on 2025 February 23 02:13:17 UTC when the asteroid was located at RA, dec = 08:04:08.66, 13:33:24.31, 1.520 au from the Sun, 0.598 au from the Earth, and had a phase angle of  $21.7^\circ$ , but only exposures in i-band were taken. During both the 2025 February 7 UTC and 2025 February 23 UTC observing dates, 200 s exposures were used for all filters, and the telescope was tracked at the rate of motion of 2024 YR<sub>4</sub>.

For this manuscript, we will focus mainly on the characterization of 2024 YR<sub>4</sub> for which we obtained observations with Gemini South on 2025 February 7 UTC. During the observations, the measured seeing in the r band was  $\sim 0.8''$  and the airmass ranged from 1.43 -1.50 during the  $\sim 2$  h 35 min observing sequence. We acquired 11 g band images, 12 r band images, 8 i band images, and 8 Z band images. The g, r, i, and Z filters changed between exposures in a rgiZrgriZgr sequence to smear out the brightness variations in the asteroid’s lightcurve and limit its effect on the color measurements. The DRAGONS image pipeline was used with bias and flat field calibration frames to detrend the data (Labrie et al. 2023). Images of 2024 YR<sub>4</sub> when it intersected a background star were discarded. A mosaic showing 2024 YR<sub>4</sub> in the co-added g, r, i, and Z frames is shown in Fig 2.

### 3. RESULTS

#### 3.1. Orbit and source population

Astrometry of 2024 YR<sub>4</sub> from observing dates was reported to the MPC (Williams 2025a,b). Additional astrometry was reported by  $\sim 440$  observations of 2024 YR<sub>4</sub> between 2024 December 25 UTC and 2025 March 1 UTC<sup>1</sup>. Table 1 shows the six orbital element solution computed by JPL HORIZONS using these observations<sup>2</sup>. The asteroid has an Apollo-type orbit with  $a > 1$  au, and a perihelion takes it inside the orbit of the Earth. The Earth minimum orbit intersection distance (MOID) according to JPL HORIZONS is  $2.82 \times 10^{-3}$  au.

The orbital and location of 2024 YR<sub>4</sub> at the time of its discovery on 2024 December 27 UTC is shown on Fig. 3 based on values from JPL Horizons<sup>3</sup>. We compared the orbit elements,  $a$ ,  $e$ ,  $i$ , and absolute magnitude  $H$  (see following Section 3.2) of 2024 YR<sub>4</sub> with the NEOMOD3 population model (Nesvorný et al. 2024), suggesting its most likely source is the 3:1 MMR with Jupiter resonance located in between the inner and central Main Belt regions at 2.5 au with a 73.9% probability. The next most likely location, with a 9.8% chance is the  $\nu_6$  resonance located at the inner edge of the Main Belt at 2.2 au. We combine our source probabilities for 2024 YR<sub>4</sub> with the NEO albedo model of Morbidelli et al. (2020) to estimate its albedo,  $p_v$ , finding a predicted value of  $\sim 0.18$ .

<sup>1</sup> [https://minorplanetcenter.net/db\\_search/show\\_object?utf8=%E2%9C%93&object\\_id=2024+YR4](https://minorplanetcenter.net/db_search/show_object?utf8=%E2%9C%93&object_id=2024+YR4), accessed on 2025 March 4 UTC.

<sup>2</sup> [https://ssd.jpl.nasa.gov/tools/sbdb\\_lookup.html#/?sstr=2024%20YR4](https://ssd.jpl.nasa.gov/tools/sbdb_lookup.html#/?sstr=2024%20YR4), solution date 2025 March 1 UTC, accessed on 2025 March 4 UTC.

<sup>3</sup> <https://ssd.jpl.nasa.gov/horizons/app.html#/>

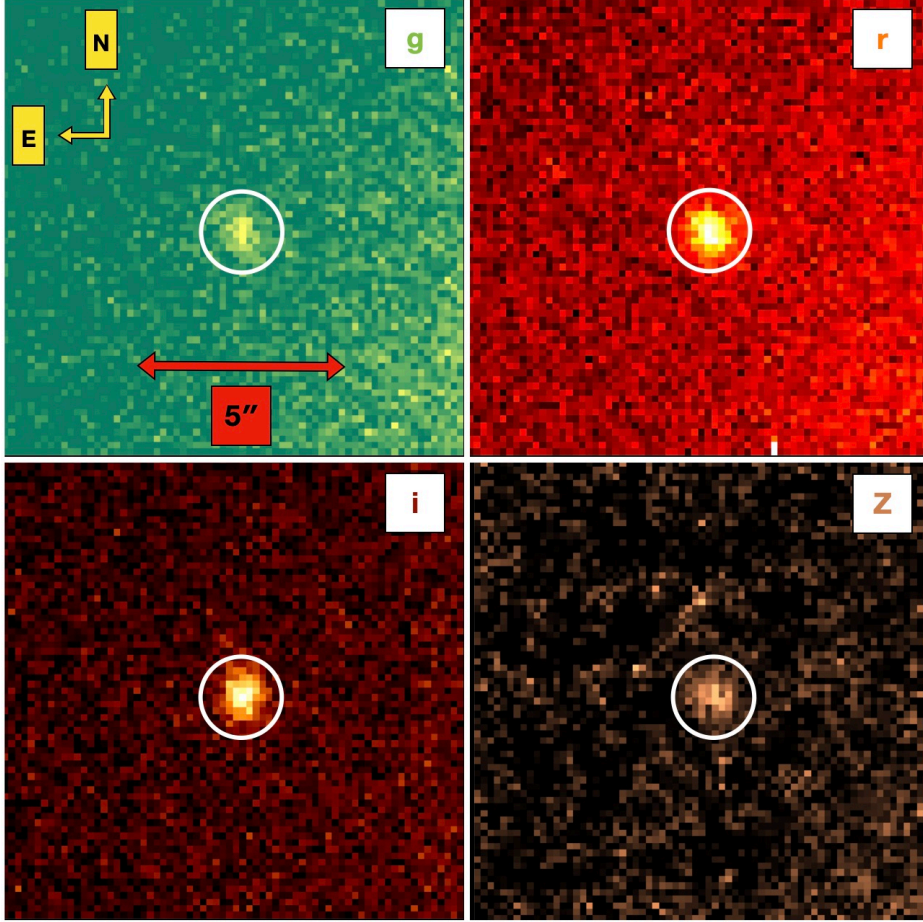


**Figure 2.** **Top left panel:** a co-add stack of 11 x 200 s g filter images of 2024 YR<sub>4</sub> with a red 5'' wide double arrow for scale. The cardinal directions are shown with yellow arrows. **Top right panel:** a co-add stack of 12 x 200 s r filter images of 2024 YR<sub>4</sub>. **Bottom left panel:** a co-add stack of 8 x 200 s i filter images of 2024 YR<sub>4</sub>. **Bottom right panel:** a co-add stack of 8 x 60 s Z filter images of 2024 YR<sub>4</sub>. The scale and orientation of the r, i, and Z band panels are the same as in the g band panel.

### 3.2. Color photometry and spectral classification

We measured the photometry of 2024 YR<sub>4</sub> in the Gemini g, r, i, and Z images using a 1.12'' aperture and a sky-median subtraction annulus with an inner and outer radius of 2.08'' and 2.88''. Local solar analog stars from the Pan-STARRS catalog (Chambers et al. 2016) were used to calibrate the photometry according to the transformations described by Tonry et al. (2012). The brightnesses per bandpass of our measured photometry are  $g = 24.01 \pm 0.09$ ,  $r = 23.31 \pm 0.04$ ,  $i = 23.06 \pm 0.04$ ,  $Z = 23.34 \pm 0.09$ . The asteroid's g-i color and spectral gradient are  $g-i = 0.95 \pm 0.10$  and  $13 \pm 33\%/100$  nm. The other multi-band color indices of 2024 YR<sub>4</sub> are  $g-r = 0.70 \pm 0.10$ ,  $r-i = 0.25 \pm 0.06$ ,  $i-Z = -0.27 \pm 0.10$ ,  $r-Z = -0.02 \pm 0.10$ , and the  $a^*$  parameter, an indicator of spectral slope defined by Ivezić et al. (2001) as  $a^* = (0.89 (g-r)) + (0.45 (r-i)) - 0.57$  is  $a^* = 0.16 \pm 0.09$ .

The  $a^*$  and  $i-z(Z)$  of 2024 YR<sub>4</sub> are plotted in Fig. 4, which has  $a^*$  and  $i-z(Z)$  on the border between S-types, which have on average  $a^* = 0.12 \pm 0.03$  and  $i-z = -0.08 \pm 0.07$ , and V-types, which have on average  $a^* = 0.15 \pm 0.11$  and  $i-z = -0.46 \pm 0.04$  (DeMeo et al. 2009). However, this is still redder compared to the Sun which has  $a^* = -0.13$  and  $i-z = 0.03$  (Willmer 2018), and C-types, which have

**Table 1.** Orbital elements of 2024 YR<sub>4</sub> taken from JPL HORIZONS (accessed on 2025 March 4 UTC) based on ~440 observations submitted to the MPC between 2024 December 25 UTC and 2025 March 1 UTC. The osculating orbital elements are shown for the Julian date (JD) epoch 2,460,800.5. The 1  $\sigma$  uncertainties are given in parentheses.

Heliocentric Elements	
Epoch (JD)	2,460,800.5
Time of perihelion, $T_p$ (JD)	2,460,636.9175586 $\pm$ (3.76x10 <sup>-5</sup> )
Semi-major axis, $a$ (au)	2.5158656 $\pm$ (2.35x10 <sup>-5</sup> )
Eccentricity, $e$	0.66154790 $\pm$ (3.35x10 <sup>-6</sup> )
Perihelion, $q$ (au)	0.851499970 $\pm$ (4.87x10 <sup>-7</sup> )
Aphelion, $Q$ (au)	4.1802311 $\pm$ (3.90x10 <sup>-5</sup> )
Inclination, $i$ ( $^\circ$ )	3.4081731 $\pm$ (1.22x10 <sup>-5</sup> )
Ascending node, $\Omega$ ( $^\circ$ )	271.36561725 $\pm$ (8.89x10 <sup>-6</sup> )
Argument of perihelion, $\omega$ ( $^\circ$ )	134.3613663 $\pm$ (1.54x10 <sup>-5</sup> )
Mean Anomaly, $M$ ( $^\circ$ )	40.402628 $\pm$ (5.7x10 <sup>-4</sup> )

on average  $a^* = -0.09 \pm 0.02$  and  $i-z = 0.02 \pm 0.03$  (DeMeo et al. 2009). Additionally, the equivalent V band brightness of 2024 YR<sub>4</sub> is  $V = 23.92 \pm 0.10$  determined by combining our g and r band measurements of the asteroid and the color transformation from (Jordi et al. 2006).

We estimate the H magnitude of 2024 YR<sub>4</sub> using our estimated V magnitude and the HG phase function (Bowell et al. 1988):

$$H = V - 5 \log_{10}(r_h \Delta) + 2.5 \log_{10} [(1 - G) \Phi_1(\alpha) + G \Phi_2(\alpha)] \quad (1)$$

where  $r_h$  is the 1.367 au heliocentric distance of 2024 YR<sub>4</sub>,  $\Delta$  is its geocentric distance of 0.399 au and  $\alpha$  is its phase angle of 14.8 $^\circ$  of 2024 YR<sub>4</sub> on 2025 February 7 UTC.  $G$  is the phase coefficient which we use the value of 0.23, the average value for S-type asteroids (Pravec et al. 2012; Vereš et al. 2015).  $\Phi_1(\alpha)$  and  $\Phi_2(\alpha)$  are the basis functions normalized at  $\alpha = 0^\circ$  described in (Bowell et al. 1988). We obtain  $H = 23.91 \pm 0.10$  in agreement from the value calculated from JPL HORIZONS of  $H = 23.96 \pm 0.28$  but caution that the uncertainty on estimate of  $H$  is underestimated due to the lack of information about the phase function (e.g., Bolin et al. 2022). Therefore, we adopt the larger uncertainty on  $H$  taken from JPL HORIZONS of  $\sim 0.3$ .

For each g, r, i, and Z filter, we compute the spectral reflectance of 2024 YR<sub>4</sub>, dividing its measured flux by the flux of a solar analog star. The reflectivity spectrum of 2024 YR<sub>4</sub> normalized to a wavelength of 550 nm is shown in Fig. 5, and features a red slope from 470 nm to 770 nm, and absorption at 880 nm. We take the approach of Bolin et al. (2023) by comparing the spectrum of 2024 YR<sub>4</sub> with the Bus-DeMeo asteroid spectral catalog (DeMeo et al. 2009) as a test of its taxonomic spectral type. We determine the reduced  $\chi^2$  statistic between the reflectance of 2024 YR<sub>4</sub> and S-type asteroids (S, Sq, Sv, Q), C-types (B, C, Cg, Cgh), X-types (X, Xc, Xe, Xk, Xn), and assorted other asteroid types (A, D, K, L, O, R, V). The closest match with the spectrum of 2024 YR<sub>4</sub> is to the R-type and Sa-type spectral classes with a reduced  $\chi^2$  of  $\sim 0.9, 1.1$ . The next closest match after R-type and Sa-type asteroids is with Sr-type asteroids with a reduced  $\chi^2$  of 1.7. By comparison, the reduced  $\chi^2$  for the spectrum of 2024 YR<sub>4</sub> with V-types and C-types are  $\sim 2.5$  and 11.8.

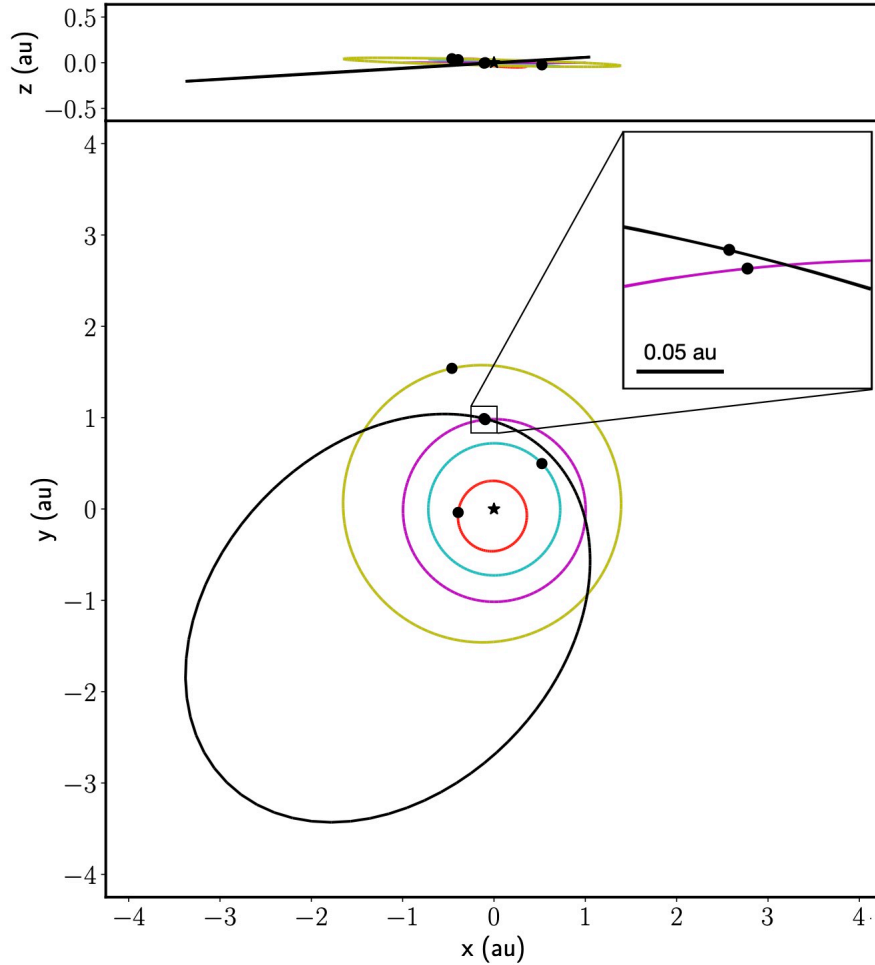


**Figure 3. Top panel:** Edge-on ecliptic view of the orbits and positions of 2024 YR<sub>4</sub> (black), Mercury (red), Venus (blue), Earth (purple), and Mars (green) at the time of the discovery of 2024 YR<sub>4</sub> on 2024 December 27 05:42:49. **Bottom panel:** the same as the top panel, except from the ecliptic pole. A close-up of the positions of 2024 YR<sub>4</sub> and the Earth is shown in an insert.

As a rough estimate of 2024 YR<sub>4</sub>'s size, we estimate its visible albedo,  $p_v$ , assuming it has similar albedo properties as other small S-complex and R-type NEOs of  $\sim 0.15$ - $0.40$  (Delbo et al. 2017). This range contains the independent albedo estimate for 2024 YR<sub>4</sub> that we obtained by using with the NEO albedo model (Morbidelli et al. 2020) of 0.18 when considering the  $\sim 0.1$  spread in albedos of small NEOs (Delbo et al. 2003). We use the albedo estimate and H magnitude of 2024 YR<sub>4</sub> to determine the diameter, D, of 2024 YR<sub>4</sub> using the equation  $D = \frac{1329}{\sqrt{p_v}} 10^{-\frac{H}{5}}$  from Harris & Lagerros (2002) arriving at  $D = 30$ - $65$  m.

### 3.3. Lightcurve photometry and shape model

The g, r, i, and Z GMOS photometry data of 2024 YR<sub>4</sub> from 2025 February 7 UTC were used to search for periodic variations in its brightness. The colors computed from Section 3.2 were used to convert the g, i, and Z data into equivalent r-band magnitudes. The combined r-band equivalent g, r, i, and Z time series lightcurve are plotted in the top panel of Fig. 6. The lightcurve shows evidence

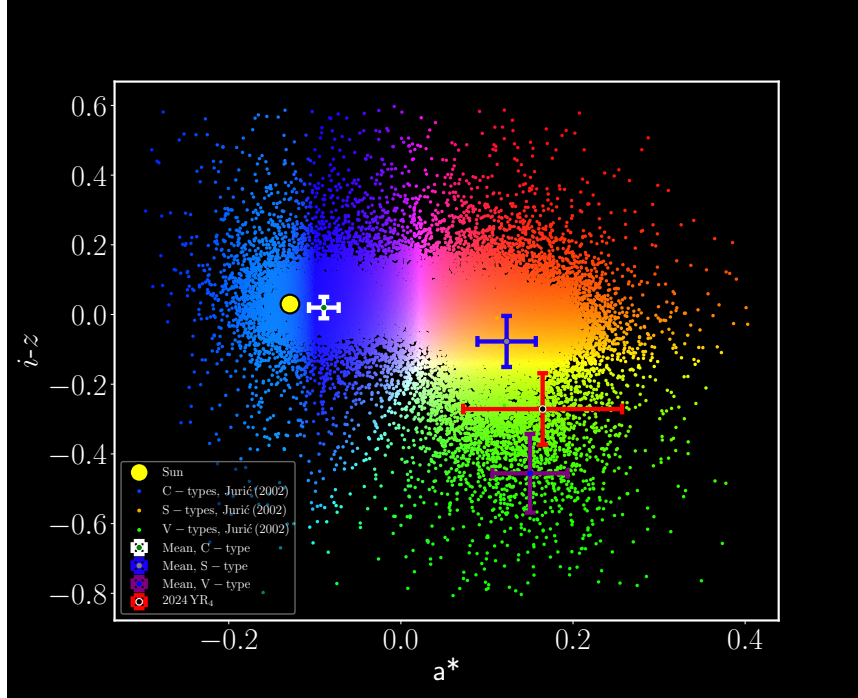


**Figure 4.** The  $a^*$  parameter vs.  $i-z(Z)$  colors of 2024 YR<sub>4</sub> from our measurements, and the  $a^*$  and  $i-z(Z)$  of C, S, and V type asteroids from Ivezić et al. (2001); Jurić et al. (2002). We use the scheme of Ivezić et al. (2002) that sets the color of data points as a function of  $a^*$  and  $i-z$  where blue symbol colors correspond to C-type asteroids, red symbol colors correspond to S-type asteroids and green symbol colors correspond to V-type asteroids. We note we use the Z magnitude of 2024 YR<sub>4</sub> in place of its Z magnitude for its  $i-z$  color calculation used in this plot. We also include the  $a^*$  and  $i-z$  determined with the mean S, V, and C-type spectra taken from DeMeo et al. (2009), and the  $a^*$  and  $i-z$  determined from the Sun’s colors (Willmer 2018).

of variations larger than the  $\sim 0.1$  mag  $1-\sigma$  photometric uncertainties of the individual data points in the lightcurve.

We take a similar approach as described by Bolin et al. (2024) to estimating the lightcurve period of the r-band equivalent data by applying a Lomb-Scargle periodogram (LS, Lomb 1976; Scargle 1982) algorithm and a phase dispersion minimization algorithm (PDM, Stellingwerf 1978) to the data. The LS and PDM algorithms result in finding an estimated lightcurve period of  $\sim 587$ - $590$ s as seen in the top and bottom panels of Fig. 7. We use the approach of (Purdum et al. 2021) estimate the uncertainty on the determined period by removing  $\sqrt{N}$  data points from the time series lightcurve and repeating our periodogram estimation of the lightcurve period  $\sim 1,000$  times, resulting in a central value of  $\sim 586$  s and a  $1 \sigma$  uncertainty estimate of  $\sim 142$  s. These period estimates imply that 2024 YR<sub>4</sub> has a double-peaked synodic rotation period of  $\sim 1172 \pm 284$  s.

The central panel of Fig. 6 shows the r-band equivalent lightcurve of 2024 YR<sub>4</sub> folded by the double-peaked rotation period of 1172 s. The result shows almost complete coverage in the lightcurve of 2024 YR<sub>4</sub> over its 1172 s rotation. We rebin the phased lightcurve of 2024 YR<sub>4</sub> into 0.075 wide bins in phase dimensional space as seen in the bottom panel of Fig. 6. We note that estimating an asteroid’s shape from a single lightcurve observation is affected by the degeneracy between viewing angle and axial ratio (e.g., Bolin et al. 2018b), therefore, we will take a multi-epoch approach to estimating the asteroid’s shape as described below.

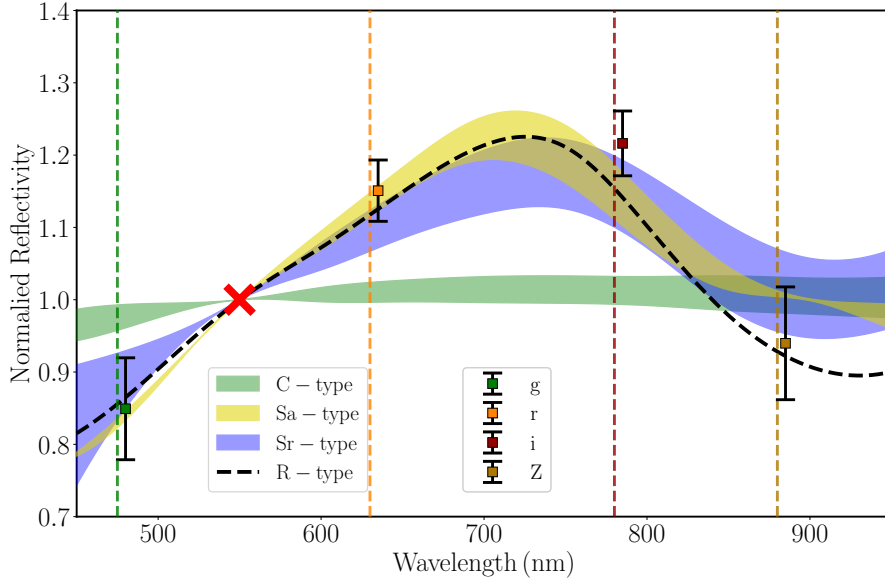
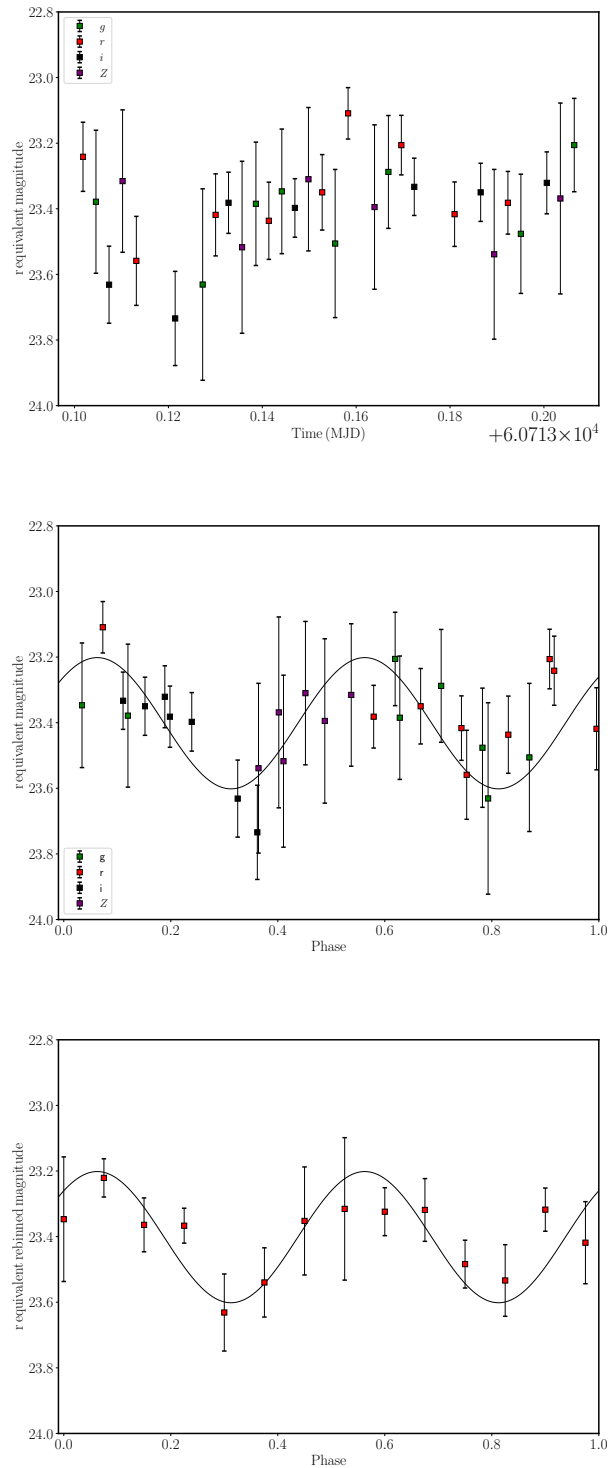


**Figure 5.** Reflectance photometric spectrum of 2024 YR<sub>4</sub> consisting of g, r, i, and Z observations of 2024 YR<sub>4</sub> on 2024 September 27 UTC. The  $\lambda_{\text{eff}}$  locations of the g, r, i, and Z filters have been plotted as vertical dashed lines. The data points for the normalized reflectivity of 2024 YR<sub>4</sub> have been offset slightly from their location in the wavelength direction. The error bars on the spectrum data points correspond to  $1\sigma$  uncertainty. The red cross indicates the spectrum has been normalized to unity at 550 nm. The spectral range of R-, Sr-, Sa- and C-type asteroids from the Bus-DeMeo asteroid taxonomic catalog (DeMeo et al. 2009) are over-plotted with the R-type spectrum most closely resembling the spectra of 2024 YR<sub>4</sub>.

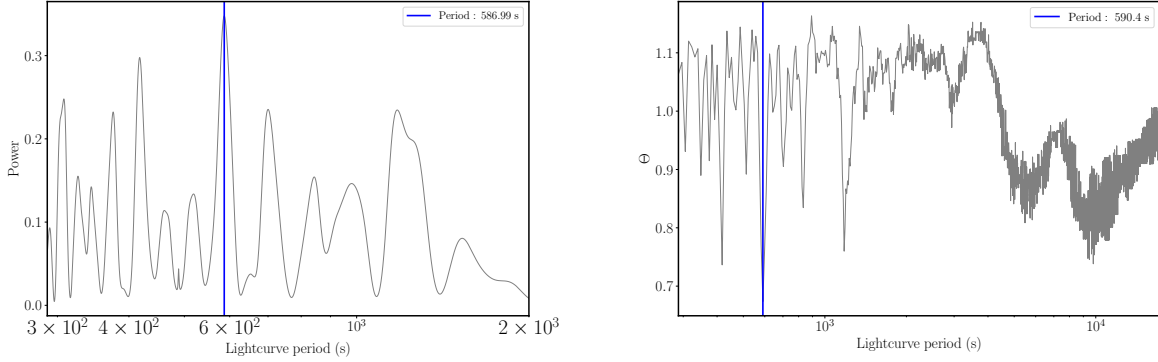
To estimate a more accurate shape for 2024 YR<sub>4</sub>, we use the lightcurve inversion method (Kaasalainen et al. 2001; Kaasalainen & Torppa 2001), which has been widely applied to derive the physical properties of small bodies, including near-Earth asteroids (NEAs). A similar approach was successfully used in the case of (3200) Phaethon, where photometric data from multiple observing geometries determined its rotational state and shape (Hanus̄ et al. 2018a).

For 2024 YR<sub>4</sub>, we used a combination of dense lightcurves obtained from Gemini (MPC observatory code, I11) we used only data in the r and g filters that are the most accurate), public data taken by the Very Large Telescope (MPC observatory code 309), and sparse photometry reported to the Minor Planet Center (MPC) that provided sufficient coverage of observing geometries. The modeling procedure followed the methodology outlined in our previous studies (Athanasopoulos et al. 2022; Hanus̄ et al. 2023).

We used photometric observations reported to the MPC: only data from observatories providing magnitude measurements with at least two decimal places were considered to ensure the highest possible accuracy. After initial modeling attempts, we further filtered out the MPC photometry, ending with three data sets. Namely, observations from multiple ATLAS (Asteroid Terrestrial-impact Last Alert System; Tonry et al. 2018) stations (MPC observatory codes (T05, T08, and W68) were combined into a single data set in the o filter, consisting of 25 individual measurements. Additional observations from the Catalina Sky Survey (Larson et al. 2003) (MPC observatory code 703), Pan-



**Figure 6. Top panel:** The r-band filter equivalent, time series lightcurve g, r, i, and Z observations of 2024 YR<sub>4</sub> taken by GMOS on 2025 February 7 UTC. The g, i, and Z data were converted to an equivalent r-band brightness by using the colors  $g-r = 0.70 \pm 0.10$ ,  $r-i = 0.25 \pm 0.06$ ,  $r-Z = -0.02 \pm 0.10$ . The error bars on the data points equal their  $1-\sigma$  photometric uncertainties. **Center panel:** The same as in the top panel, but the data have been phased by a double-peaked rotation period of 1172 s. A sinusoidal lightcurve model with a double-peaked period of  $\sim 1172$  s and amplitude of 0.40 magnitudes is plotted in black. **Bottom panel:** the same as in the center panel, except that the data have been re-binned in with 0.075 wide bins in phase dimensional space.

**Figure 7.**

Left panel: Lomb-Scargle periodogram of lightcurve period vs. spectral power (Lomb 1976) for the g filter data from the 2024 September 27 UTC Gemini N/GMOS observations. A peak in power is located at a single-peaked lightcurve period of 587 s. **Right panel:** Phase dispersion minimization analysis of lightcurve rotation period vs.  $\Theta$  metric (Stellingwerf 1978). The  $\Theta$  metric is minimized at single-peaked rotation periods of 1150 s, similar to the  $1320 \pm 227$  s period found with the Lomb-Scargle Periodogram.

STARRS2 (MPC observatory code F52) (Chambers et al. 2016) stations combined together in the G filter finalized the sparse dataset.

The photometric data were processed following the methodology outlined in Hanuš et al. (2011) to prepare them for lightcurve inversion. This procedure included transformation to fluxes, epoch light-travel time correction, flux normalization to unit distance to the Sun and the observer, and unity. Any outliers or measurements affected by systematic errors were identified and removed.

Dense photometric observations of 2024 YR<sub>4</sub> were obtained from the European Southern Observatory (ESO) Science Archive as part of a long-term monitoring program (ESO Program ID 113.2690.002, PI Hainaut). The program, conducted in Service Mode at VLT UT1-Antu, supports the ESA Space Situational Awareness Near-Earth Objects Protection Program, which aims to characterize the physical properties of potentially hazardous asteroids. The observations were taken with the FORS2 instrument on 2025 January 21 UTC.

The VLT data are publicly available, and we retrieved them from the ESO database as raw images. The data were processed using the MPO Canopus software package, following standard photometric reduction procedures (Warner et al. 2009). Bias and flat-field corrections were applied to all frames, followed by aperture photometry extraction, calibrated against known field stars to ensure accurate magnitude measurements.

The available photometric dataset spans 42 days of observations, covering a range of phase angles from  $45.7^\circ$  to  $14.8^\circ$ , which is critical for constraining the shape model. Table A.1 summarizes the complete list of photometric measurements, including observation epochs, filter bands, and sources.

We conducted a broad period search within the range of 0.15 to 0.50 hours, encompassing the suspected synodic period of approximately  $\sim 0.32$  hours derived from the photometric dataset. A well-defined minimum was identified in the periodogram at  $P_{\text{sid}} = 0.32439$  hours (1168s) (Figure 8). This solution remains stable against variations in the relative weighting of the individual datasets, confirming its robustness.

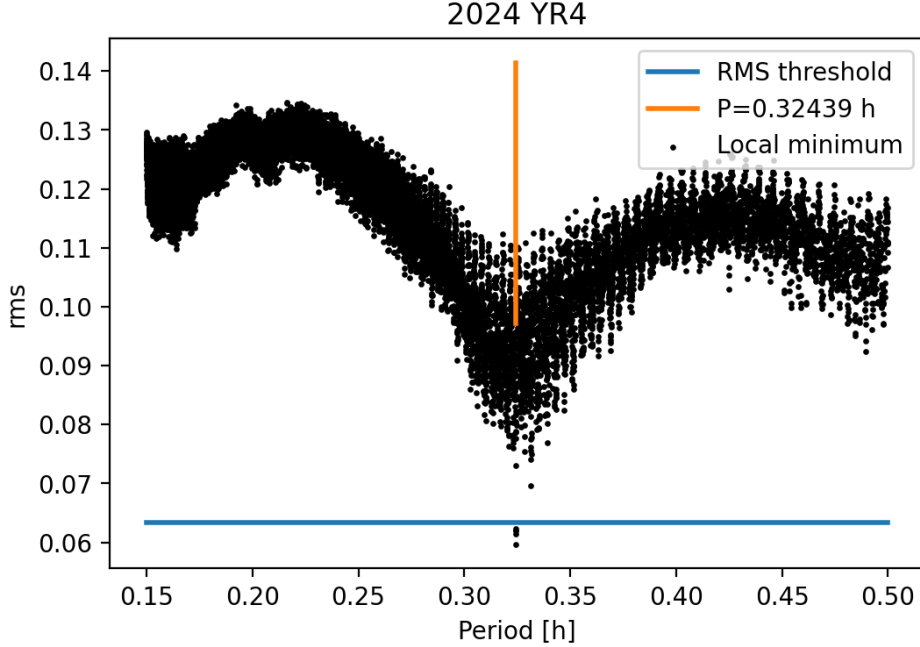


**Figure 8.** The periodogram of 2024 YR4, computed near the suspected synodic period. The minimum at  $P_{\text{sid}} = 0.32439$  hours, indicated by the vertical line, corresponds to the global minimum. The horizontal line represents the RMS threshold, indicating the statistical significance of the minimum.

Adopting this sidereal period, we explored possible spin-vector orientations by testing a wide range of initial values isotropically distributed on a sphere. The results indicate a degree of sensitivity to the chosen data weighting. Several pole solutions were tested using different relative weight configurations, with the most prominent solution found at an ecliptic longitude and latitude of approximately  $\lambda = 42^\circ$  and  $\beta = -25^\circ$ , respectively. This particular solution satisfies physical constraints, ensuring that the derived shape model rotates around its principal axis with maximum momentum of inertia. While alternative pole solutions cannot be entirely excluded, this solution appears to be the most plausible. This solution will be included in the Database of Asteroid Models from Inversion Techniques (DAMIT) lightcurve inversion software package (Durech et al. 2015).

Figure 9 presents the fit to the photometric data, incorporating dense lightcurves obtained from VLT and Gemini in the  $r$  and  $g$  filters, along with sparse photometric measurements from ATLAS, the Catalina Sky Survey, and Pan-STARRS. The derived shape of 2024 YR4 is notably peculiar, resembling a highly flattened spheroid with nearly equal equatorial dimensions (Fig. 8).

#### 4. DISCUSSION AND CONCLUSIONS

The properties of 2024 YR<sub>4</sub> are similar to other small NEOs, that it has a S-complex composition, most likely originated from a resonances located inner Main Belt, and likely has moderate reflective properties implying a size of  $\sim 42$  m. The exact origin within the Main Belt seems less clear, though a clue may lie in its spin-vector orientation. As recent asteroid lightcurve spin-vector studies have shown, the spin direction of an asteroid can affect the way an asteroid’s orbit evolves due to the thermal recoil Yarkovsky effect, with prograde asteroids drifting outward, and retrograde asteroids drifting inwards (Bolin et al. 2018a; Hanuš et al. 2018b; Athanasopoulos et al. 2022). Since the spin direction of 2024 YR<sub>4</sub> is retrograde with its  $-39^\circ$  ecliptic latitude, an origin from the inner Main

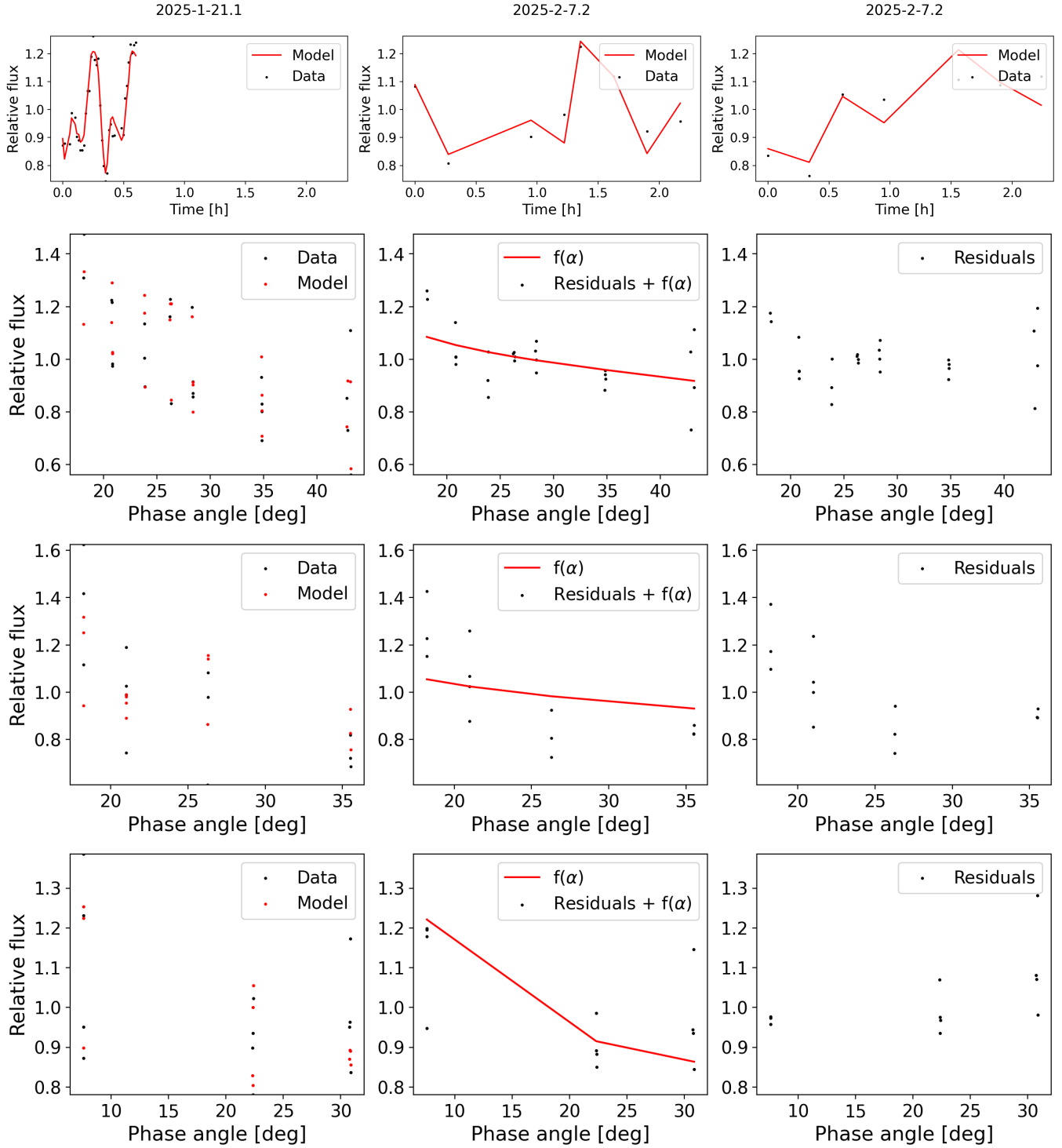


**Figure 9.** Lightcurve fit of 2024 YR<sub>4</sub>, showing dense photometric observations from VLT and Gemini in the *r* and *g* filters (top panels), and sparse datasets from ATLAS, Catalina Sky Survey, and Pan-STARRS (bottom three panels). The best-fit model is overlaid.

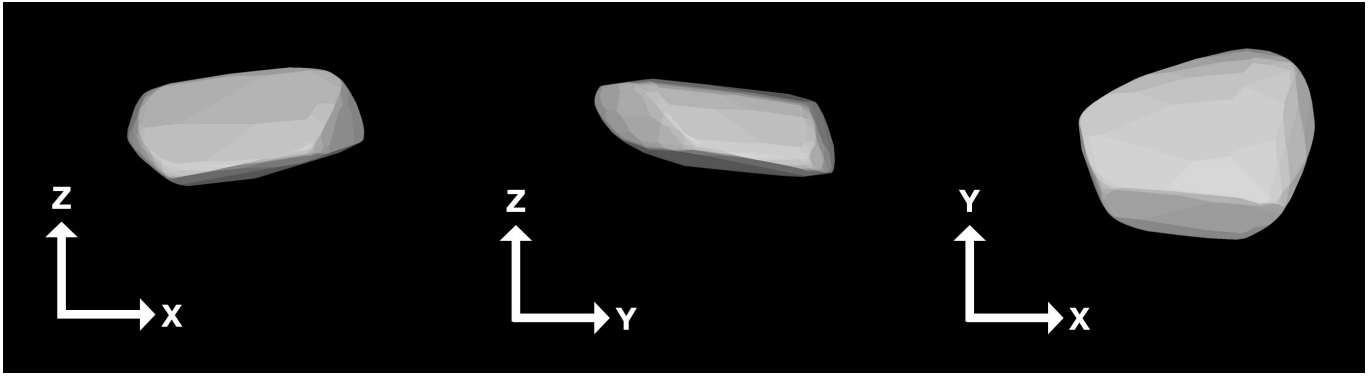


**Figure 10.** Convex shape model of 2024 YR<sub>4</sub> in three orthogonal views obtained using publicly available photometry of 2024 YR<sub>4</sub> from the Minor Planet Center archive, VLT archive and Gemini. The X vs. Z and Y vs. Z views show the edge on view of the asteroid with the spin axis pointing in the Z direction (ecliptic longitude and latitude equal to 42° and -25 degrees°). The asteroid is viewed from a pole-on view in the X vs. Y view.

Belt since its retrograde spin would cause it to drift inwards away from the 3:1 MMR at 2.5 au, its most likely escape path into the NEO population. Therefore, its suspected retrograde spin may imply that its original location was the central Main Belt, located at 2.52 au to 2.82 au from the Sun (Nesvorný et al. 2015). This would take 2024 YR<sub>4</sub>’s origins away from the inner Main Belt where S-types dominate to the central Main Belt where C-types are more plentiful seemingly in tension with its taxonomic type (DeMeo & Carry 2014). However, several S-type families are located near the 3:1 MMR in the central Main Belt, such as the Rafita family located at 2.58 au, which could be a candidate source family for 2024 YR<sub>4</sub>.

## ACKNOWLEDGMENTS

This study is based on observations obtained at the international Gemini Observatory, a program of NSF’s NOIRLab, which is managed by the Association of Universities for Research in Astronomy (AURA) under a cooperative agreement with the National Science Foundation on behalf of the Gemini Observatory partnership.

Gemini Observatory is located on Maunakea, land of the Kānaka Maoli people, and a mountain of considerable cultural, natural, and ecological significance to the indigenous Hawaiian people. The authors wish to acknowledge the importance and reverence of Maunakea and express gratitude for the opportunity to conduct observations from the mountain.

This work has been supported by the grant 25-16789S of the Czech Science Foundation.

The authors wish to thank Matthew Belyakov for help with the observations of 2024 YR<sub>4</sub>, and Mauro Barbieri for help with searching the VLT data archive. The authors also wish to thank K. Wierzos, and C. Fuls for their help with measuring the astrometry from the Gemini images and submitting it to the MPC. The authors also wish to thank the team members of the Catalina Sky Survey, the Panoramic Survey Telescope and Rapid Response System, an ATLAS for submitting observations of 2024 YR<sub>4</sub> to the MPC which were used in this work.

This research has made use of data and/or services provided by the International Astronomical Union’s Minor Planet Center.

*Facility:* ATLAS, Gemini:South, VLT:Antu

## REFERENCES

- Athanasopoulos, D., Hanuš, J., Avdellidou, C., et al. 2022, *A&A*, 666, A116, doi: [10.1051/0004-6361/202243905](https://doi.org/10.1051/0004-6361/202243905)
- Avdellidou, C., Delbo, M., Morbidelli, A., et al. 2022, *A&A*, 665, L9, doi: [10.1051/0004-6361/202244590](https://doi.org/10.1051/0004-6361/202244590)
- Binzel, R. P., Reddy, V., & Dunn, T. L. 2015, *The Near-Earth Object Population: Connections to Comets, Main-Belt Asteroids, and Meteorites*, 243–256
- Binzel, R. P., Morbidelli, A., Merouane, S., et al. 2010, *Nature*, 463, 331, doi: [10.1038/nature08709](https://doi.org/10.1038/nature08709)
- Binzel, R. P., DeMeo, F. E., Turtelboom, E. V., et al. 2019, *Icarus*, 324, 41, doi: [10.1016/j.icarus.2018.12.035](https://doi.org/10.1016/j.icarus.2018.12.035)
- Bolin, B. T., Denneau, L., Abron, L.-M., et al. 2025, *ApJL*, 978, L37, doi: [10.3847/2041-8213/ada1d0](https://doi.org/10.3847/2041-8213/ada1d0)
- Bolin, B. T., Ghosal, M., & Jedicke, R. 2024, *MNRAS*, 527, 1633, doi: [10.1093/mnras/stad3227](https://doi.org/10.1093/mnras/stad3227)
- Bolin, B. T., Morbidelli, A., & Walsh, K. J. 2018a, *A&A*, 611, A82, doi: [10.1051/0004-6361/201732079](https://doi.org/10.1051/0004-6361/201732079)
- Bolin, B. T., Noll, K. S., Caiazzo, I., Fremling, C., & Binzel, R. P. 2023, *Icarus*, 400, 115562, doi: [10.1016/j.icarus.2023.115562](https://doi.org/10.1016/j.icarus.2023.115562)
- Bolin, B. T., Weaver, H. A., Fernandez, Y. R., et al. 2018b, *ApJL*, 852, L2, doi: [10.3847/2041-8213/aaa0c9](https://doi.org/10.3847/2041-8213/aaa0c9)
- Bolin, B. T., Fremling, C., Holt, T. R., et al. 2020, *ApJL*, 900, L45, doi: [10.3847/2041-8213/abae69](https://doi.org/10.3847/2041-8213/abae69)
- Bolin, B. T., Fernandez, Y. R., Lisse, C. M., et al. 2021, *AJ*, 161, 116, doi: [10.3847/1538-3881/abd94b](https://doi.org/10.3847/1538-3881/abd94b)
- Bolin, B. T., Ahumada, T., van Dokkum, P., et al. 2022, *MNRAS*, 517, L49, doi: [10.1093/mnrasl/slac089](https://doi.org/10.1093/mnrasl/slac089)
- Bowell, E., Hapke, B., Domingue, D., et al. 1988, *Asteroids II*, 399
- Bus, S. J., & Binzel, R. P. 2002, *Icarus*, 158, 146, doi: [10.1006/icar.2002.6856](https://doi.org/10.1006/icar.2002.6856)
- Casali, M., Adamson, A., Alves de Oliveira, C., et al. 2007, *A&A*, 467, 777, doi: [10.1051/0004-6361:20066514](https://doi.org/10.1051/0004-6361:20066514)
- Chambers, K. C., Magnier, E. A., Metcalfe, N., et al. 2016, *ArXiv e-prints*, <https://arxiv.org/abs/1612.05560>
- Cohen, B. A., van der Bogert, C. H., Bottke, W. F., et al. 2023, *Reviews in Mineralogy and Geochemistry*, 89, 373, doi: [10.2138/rmg.2023.89.09](https://doi.org/10.2138/rmg.2023.89.09)
- Delbo, M., Harris, A. W., Binzel, R. P., Pravec, P., & Davies, J. K. 2003, *Icarus*, 166, 116, doi: [10.1016/j.icarus.2003.07.002](https://doi.org/10.1016/j.icarus.2003.07.002)
- Delbo, M., Walsh, K., Bolin, B., Avdellidou, C., & Morbidelli, A. 2017, *Science*, 357, 1026, doi: [10.1126/science.aam6036](https://doi.org/10.1126/science.aam6036)
- DeMeo, F. E., Binzel, R. P., Slivan, S. M., & Bus, S. J. 2009, *Icarus*, 202, 160, doi: [10.1016/j.icarus.2009.02.005](https://doi.org/10.1016/j.icarus.2009.02.005)
- DeMeo, F. E., & Carry, B. 2013, *Icarus*, 226, 723, doi: [10.1016/j.icarus.2013.06.027](https://doi.org/10.1016/j.icarus.2013.06.027)
- . 2014, *Nature*, 505, 629, doi: [10.1038/nature12908](https://doi.org/10.1038/nature12908)
- Denneau, L., Siverd, R., Tonry, J., et al. 2024, *Minor Planet Electronic Circulars*, 2024-Y140
- Durech, J., Carry, B., Delbo, M., Kaasalainen, M., & Viikinkoski, M. 2015, *Asteroid Models from Multiple Data Sources*, ed. P. Michel, F. E. DeMeo, & W. F. Bottke, 183–202
- Farinella, P., Gonczi, R., Froeschle, C., & Froeschle, C. 1993, *Icarus*, 101, 174, doi: [10.1006/icar.1993.1016](https://doi.org/10.1006/icar.1993.1016)
- Fukugita, M., Ichikawa, T., Gunn, J. E., et al. 1996, *AJ*, 111, 1748, doi: [10.1086/117915](https://doi.org/10.1086/117915)
- Granvik, M., Jedicke, R., Bolin, B., Chyba, M., & Patterson, G. 2013, *Earth's Temporarily-Captured Natural Satellites - The First Step towards Utilization of Asteroid Resources*, ed. V. Badescu, 151–167
- Granvik, M., Morbidelli, A., Vokrouhlický, D., et al. 2017, *A&A*, 598, A52, doi: [10.1051/0004-6361/201629252](https://doi.org/10.1051/0004-6361/201629252)
- Granvik, M., & Walsh, K. J. 2024, *ApJL*, 960, L9, doi: [10.3847/2041-8213/ad151b](https://doi.org/10.3847/2041-8213/ad151b)

- Granvik, M., Morbidelli, A., Jedicke, R., et al. 2018, *Icarus*, 312, 181, doi: [10.1016/j.icarus.2018.04.018](https://doi.org/10.1016/j.icarus.2018.04.018)
- Hanuš, J., Ďurech, J., Brož, M., et al. 2011, *A&A*, 530, A134, doi: [10.1051/0004-6361/201116738](https://doi.org/10.1051/0004-6361/201116738)
- Hanuš, J., Delbo, M., Alí-Lagoa, V., et al. 2018, *Icarus*, 299, 84, doi: [10.1016/j.icarus.2017.07.007](https://doi.org/10.1016/j.icarus.2017.07.007)
- Hanuš, J., Vokrouhlický, D., Nesvorný, D., et al. 2023, *A&A*, 679, A56, doi: [10.1051/0004-6361/202346022](https://doi.org/10.1051/0004-6361/202346022)
- Hanuš, J., Vokrouhlický, D., Delbo, M., et al. 2018a, *A&A*, 620, L8, doi: [10.1051/0004-6361/201834228](https://doi.org/10.1051/0004-6361/201834228)
- Hanuš, J., Delbo, M., Alí-Lagoa, V., et al. 2018b, *Icarus*, 299, 84, doi: [10.1016/j.icarus.2017.07.007](https://doi.org/10.1016/j.icarus.2017.07.007)
- Harris, A. W., & Lagerros, J. S. V. 2002, *Asteroids III*, 205
- Hodgkin, S. T., Irwin, M. J., Hewett, P. C., & Warren, S. J. 2009, *MNRAS*, 394, 675, doi: [10.1111/j.1365-2966.2008.14387.x](https://doi.org/10.1111/j.1365-2966.2008.14387.x)
- Hook, I. M., Jørgensen, I., Allington-Smith, J. R., et al. 2004, *PASP*, 116, 425, doi: [10.1086/383624](https://doi.org/10.1086/383624)
- Ivezić, Ž., Tabachnik, S., Rafikov, R., et al. 2001, *AJ*, 122, 2749, doi: [10.1086/323452](https://doi.org/10.1086/323452)
- Ivezić, Ž., Lupton, R. H., Jurić, M., et al. 2002, *AJ*, 124, 2943, doi: [10.1086/344077](https://doi.org/10.1086/344077)
- Jedicke, R., Hermosin, P., Sercel, J., et al. 2022, *Planet. Space Sci.*, 211, 105407, doi: [10.1016/j.pss.2021.105407](https://doi.org/10.1016/j.pss.2021.105407)
- Jordi, K., Grebel, E. K., & Ammon, K. 2006, *A&A*, 460, 339, doi: [10.1051/0004-6361:20066082](https://doi.org/10.1051/0004-6361:20066082)
- Jurić, M., Ivezić, Ž., Lupton, R. H., et al. 2002, *AJ*, 124, 1776, doi: [10.1086/341950](https://doi.org/10.1086/341950)
- Kaasalainen, M., & Torppa, J. 2001, *Icarus*, 153, 24, doi: [10.1006/icar.2001.6673](https://doi.org/10.1006/icar.2001.6673)
- Kaasalainen, M., Torppa, J., & Muinonen, K. 2001, *Icarus*, 153, 37, doi: [10.1006/icar.2001.6674](https://doi.org/10.1006/icar.2001.6674)
- Labrie, K., Simpson, C., Cardenas, R., et al. 2023, *Research Notes of the American Astronomical Society*, 7, 214, doi: [10.3847/2515-5172/ad0044](https://doi.org/10.3847/2515-5172/ad0044)
- Larson, S., Beshore, E., Hill, R., et al. 2003, in *AAS/Division for Planetary Sciences Meeting Abstracts*, Vol. 35, AAS/Division for Planetary Sciences Meeting Abstracts #35, 36.04
- Lomb, N. R. 1976, *Ap&SS*, 39, 447, doi: [10.1007/BF00648343](https://doi.org/10.1007/BF00648343)
- Mazrouei, S., Ghent, R. R., Bottke, W. F., Parker, A. H., & Gernon, T. M. 2019, *Science*, 363, 253, doi: [10.1126/science.aar4058](https://doi.org/10.1126/science.aar4058)
- Morbidelli, A., Delbo, M., Granvik, M., et al. 2020, *Icarus*, 340, 113631, doi: [10.1016/j.icarus.2020.113631](https://doi.org/10.1016/j.icarus.2020.113631)
- Nesvorný, D., Brož, M., & Carruba, V. 2015, *Asteroids IV*, 297, doi: [10.2458/azu\\_uapress.9780816530595-ch016](https://doi.org/10.2458/azu_uapress.9780816530595-ch016)
- Nesvorný, D., Deienno, R., Bottke, W. F., et al. 2023, *AJ*, 166, 55, doi: [10.3847/1538-3881/ace040](https://doi.org/10.3847/1538-3881/ace040)
- Nesvorný, D., Vokrouhlický, D., Shelly, F., et al. 2024, *Icarus*, 417, 116110, doi: [10.1016/j.icarus.2024.116110](https://doi.org/10.1016/j.icarus.2024.116110)
- Pravec, P., Harris, A. W., Kušnirák, P., Galád, A., & Hornoch, K. 2012, *Icarus*, 221, 365, doi: [10.1016/j.icarus.2012.07.026](https://doi.org/10.1016/j.icarus.2012.07.026)
- Purdum, J. N., Lin, Z.-Y., Bolin, B. T., et al. 2021, *ApJL*, 911, L35, doi: [10.3847/2041-8213/abf2ca](https://doi.org/10.3847/2041-8213/abf2ca)
- Scargle, J. D. 1982, *ApJ*, 263, 835, doi: [10.1086/160554](https://doi.org/10.1086/160554)
- Stellingwerf, R. F. 1978, *ApJ*, 224, 953, doi: [10.1086/156444](https://doi.org/10.1086/156444)
- Tonry, J. L., Stubbs, C. W., Lykke, K. R., et al. 2012, *ApJ*, 750, 99, doi: [10.1088/0004-637X/750/2/99](https://doi.org/10.1088/0004-637X/750/2/99)
- Tonry, J. L., Denneau, L., Heinze, A. N., et al. 2018, *PASP*, 130, 064505, doi: [10.1088/1538-3873/aabadf](https://doi.org/10.1088/1538-3873/aabadf)
- Vereš, P., Jedicke, R., Fitzsimmons, A., et al. 2015, *Icarus*, 261, 34, doi: [10.1016/j.icarus.2015.08.007](https://doi.org/10.1016/j.icarus.2015.08.007)
- Vokrouhlický, D., Bottke, W. F., Chesley, S. R., Scheeres, D. J., & Statler, T. S. 2015, *Asteroids IV*, 509, doi: [10.2458/azu\\_uapress.9780816530595-ch027](https://doi.org/10.2458/azu_uapress.9780816530595-ch027)
- Warner, B. D., Harris, A. W., & Pravec, P. 2009, *Icarus*, 202, 134, doi: [10.1016/j.icarus.2009.02.003](https://doi.org/10.1016/j.icarus.2009.02.003)
- Williams, G. V. 2025a, *Minor Planet Electronic Circulars*, 2025-D145
- . 2025b, *Minor Planet Electronic Circulars Supplement*, 2321551
- Willmer, C. N. A. 2018, *ApJS*, 236, 47, doi: [10.3847/1538-4365/aabfdf](https://doi.org/10.3847/1538-4365/aabfdf)
- Wisdom, J. 1983, *Icarus*, 56, 51, doi: [10.1016/0019-1035\(83\)90127-6](https://doi.org/10.1016/0019-1035(83)90127-6)

## APPENDIX

**Table A1.** Summary of 2024 YR<sub>4</sub> photometry from between 2024 December 27 and 2025 February 7 UTC.

Date <sup>1</sup> (MJD UTC)	Mag <sup>2</sup>	Mag unc. <sup>3</sup> (s)	Obs. Code <sup>4</sup>
60671.23807315	16.54	0.03	W68
60671.24033426	15.80	0.03	W68
60671.26732187	16.28	0.03	W68
60671.27464815	16.12	0.03	W68
60672.34588600	17.31	0.10	703
60672.35043700	17.12	0.10	703
60672.35271000	17.26	0.10	703
60672.48815185	17.10	0.05	T05
60672.48996875	17.30	0.05	T05
60672.49358611	17.14	0.03	T05
60672.49902662	16.98	0.03	T05
60673.52814200	17.49	0.13	F52
60673.54101000	17.13	0.13	F52
60673.55386300	17.35	0.13	F52
60673.56663600	17.37	0.13	F52
60674.40934711	18.05	0.07	T08
60674.41258137	18.07	0.07	T08
60674.41536956	18.00	0.05	T08
60674.44491667	17.72	0.04	T08
60675.28366667	18.04	0.09	W68
60675.28781644	18.45	0.09	W68
60675.30947500	18.27	0.27	703
60675.31180000	18.38	0.27	703
60675.31644000	18.90	0.27	703
60675.32319479	18.04	0.07	W68
60675.34909931	18.11	0.12	W68
60676.55924286	18.80	0.11	T05
60676.56982976	18.68	0.09	T05
60676.57969515	18.55	0.11	T05
60677.43338700	18.72	0.11	F52
60677.44491300	18.82	0.11	F52
60677.45652500	19.02	0.11	F52
60677.46819900	18.87	0.11	F52
60678.32803200	19.25	0.18	703

*Continued on next page*

Table A1 – *Continued from previous page*

Date <sup>1</sup> (MJD UTC)	Mag <sup>2</sup>	Mag unc. <sup>3</sup> (s)	Obs. Code <sup>4</sup>
60678.33011000	19.60	0.18	703
60678.33218800	19.29	0.18	703
60678.33426500	19.09	0.18	703
60678.45297894	19.23	0.15	T08
60678.45618218	19.24	0.15	T08
60678.45939005	19.00	0.13	T08
60678.48978009	19.00	0.12	T08
60680.33804700	19.22	0.17	703
60680.34013000	19.37	0.17	703
60680.34428800	19.63	0.17	703
60680.39489045	19.24	0.17	T05
60680.44102885	19.38	0.19	T05
60696.11607700	21.55	0.05	309
60696.11669800	21.54	0.05	309
60696.11851100	21.55	0.05	309
60696.11911300	21.42	0.04	309
60696.12032800	21.43	0.04	309
60696.12093800	21.52	0.05	309
60696.12155200	21.53	0.05	309
60696.12215700	21.57	0.05	309
60696.12275900	21.57	0.05	309
60696.12337200	21.55	0.05	309
60696.12398200	21.42	0.04	309
60696.12458800	21.34	0.04	309
60696.12520900	21.34	0.04	309
60696.12581400	21.22	0.04	309
60696.12642500	21.15	0.03	309
60696.12703500	21.23	0.04	309
60696.12764300	21.24	0.04	309
60696.12826200	21.22	0.04	309
60696.12887900	21.39	0.04	309
60696.12948400	21.53	0.05	309
60696.13008500	21.65	0.05	309
60696.13069600	21.73	0.05	309
60696.13130900	21.69	0.05	309
60696.13191400	21.49	0.04	309
60696.13253600	21.46	0.04	309
60696.13314100	21.51	0.04	309

*Continued on next page*

Table A1 – *Continued from previous page*

Date <sup>1</sup> (MJD UTC)	Mag <sup>2</sup>	Mag unc. <sup>3</sup> (s)	Obs. Code <sup>4</sup>
60696.13375100	21.51	0.05	309
60696.13619300	21.48	0.04	309
60696.13679900	21.51	0.04	309
60696.13740900	21.36	0.04	309
60696.13801400	21.32	0.04	309
60696.13862800	21.24	0.04	309
60696.13923000	21.18	0.03	309
60696.13984300	21.21	0.04	309
60696.14045700	21.18	0.03	309
60696.14107800	21.17	0.03	309
60697.33390700	22.01	0.20	F52
60697.34534000	21.92	0.20	F52
60697.35679700	21.51	0.20	F52
60697.36823700	21.64	0.20	F52
60713.10456210	23.38	0.22	I11
60713.12729625	23.63	0.29	I11
60713.13864208	23.38	0.19	I11
60713.14415887	23.35	0.19	I11
60713.15552038	23.51	0.23	I11
60713.16686808	23.29	0.17	I11
60713.19509238	23.48	0.18	I11
60713.20646260	23.21	0.14	I11
60713.10180008	23.24	0.11	I11
60713.11316511	23.56	0.14	I11
60713.14139774	23.44	0.12	I11
60713.15275886	23.35	0.12	I11
60713.15827524	23.11	0.08	I11
60713.16962233	23.21	0.09	I11
60713.18097070	23.42	0.10	I11
60713.19232942	23.38	0.10	I11
60713.10734983	23.63	0.12	I11
60713.12143592	23.73	0.14	I11
60713.13280506	23.38	0.09	I11
60713.14694628	23.40	0.09	I11
60713.17237680	23.33	0.09	I11
60713.18652172	23.35	0.09	I11
60713.20061316	23.32	0.09	I11
60713.11023326	23.32	0.22	I11

*Continued on next page*

Table A1 – *Continued from previous page*

Date <sup>1</sup> (MJD UTC)	Mag <sup>2</sup>	Mag unc. <sup>3</sup> (s)	Obs. Code <sup>4</sup>
60713.13568818	23.52	0.26	I11
60713.14983347	23.31	0.22	I11
60713.16391275	23.39	0.25	I11
60713.18940483	23.54	0.26	I11
60713.20350766	23.37	0.29	I11

**Table A1.** Columns: (1) observation date; (2) r-band equivalent magnitude; (3) 1- $\sigma$  magnitude uncertainty (4) observatory code

---